Pre-flight performance of the ion energy mass spectrum analyzer for the Martian Moons eXploration (MMX) mission

Shoichiro Yokota, Ayako Matsuoka, Naofumi Murata, Yoshifumi Saito, Kazushi Asamura, Satoshi Kasahara, Dominique Delcourt, Lina Z Hadid, Naoki Terada, Kunihiro Keika, et al.

Yokota *et al.*
Progress in Earth and Planetary Science (2025) 12:51
https://doi.org/10.1186/s40645-025-00718-2

Progress in Earth and Planetary Science

RESEARCH ARTICLE

Open Access

Pre-flight performance of the ion energy mass spectrum analyzer for the Martian Moons eXploration (MMX) mission

Shoichiro Yokota[1*], Ayako Matsuoka[2], Naofumi Murata[3], Yoshifumi Saito[4], Kazushi Asamura[4], Satoshi Kasahara[5], Dominique Delcourt[6,7], Lina Z. Hadid[6], Naoki Terada[8], Kunihiro Keika[5], Yuki Harada[2], Hiromu Nakagawa[8], Kei Masunaga[9], Shotaro Sakai[11], Yoshifumi Futaana[10], Shun Imajo[2], Kanako Seki[5], Masaki N. Nishino[4] and Yuki Kitamura[1]

Abstract

An ion energy mass spectrum analyzer was developed for the Martian Moons eXploration (MMX) mission to measure the three-dimensional velocity distribution function and mass profile of low-energy ions around the Mars-Moon system. The hemispheric field-of-view (FOV) is acquired by a pair of angular scanning deflectors, and the energy/charge and mass/charge are determined for each ion by an electrostatic analyzer and a linear-electric-field (LEF) time-of-flight (TOF) analyzer, respectively, with an enhanced mass resolution of $m/\Delta m \sim 100$. The ion analyzer, together with magnetometers, constitutes the mass spectrum analyzer (MSA), one of the scientific instruments on board the MMX spacecraft. This paper describes the instrumentation of the ion analyzer, and results of the performance tests of its flight model (FM).

Keywords Martian Moons eXploration (MMX), Phobos, Mars, Mass spectrum analyzer, Ion analyzer, Time-of-flight, Secondary ions, The solar wind, Atmospheric ions

1 Introduction

The Martian Moons eXploration (MMX) mission planned by the Japan Aerospace Exploration Agency (JAXA) is now scheduled for launch in 2026, arrival at Mars in 2027, and sample return to the Earth in 2031. The scientific objectives are to clarify the origins of the Martian moons, and to understand the physical mechanisms and co-evolution history of the Martian–moons system (Kuramoto et al. 2021). The MMX spacecraft is equipped with several remote-sensing and in situ observing instruments (Barucci et al. 2021; Cho et al. 2021; Kameda et al. 2021; Kobayashi et al. 2018; Lawrence et al. 2019; Michel et al. 2022; Senshu et al. 2021; Yokota et al. 2021) to achieve such scientific objectives independently of sample analyses (Usui et al. 2020). In its observations, the MMX spacecraft will orbit Mars with Phobos, simultaneously covering a wide area of Phobos' surface in

*Correspondence:
Shoichiro Yokota
yokota@ess.sci.osaka-u.ac.jp
[1] Osaka University, Machikaneyama-cho, Toyonaka 560-0043, Japan
[2] Kyoto University, Kitashirakawaoiwake-cho, Sakyo-ku, Kyoto 606-8502, Japan
[3] Japan Aerospace Exploration Agency, Tsukuba, Ibaraki 305-8505, Japan
[4] Institute of Space and Astronautical Science, Japan Aerospace Exploration Agency, Yoshinodai, Chuo-ku, Sagamihara 252-5210, Japan
[5] The University of Tokyo, Hongo, Bunkyo-ku 113-0033, Japan
[6] LPP, CNRS, Observatoire de Paris, Sorbonne Universite, Universite Paris Saclay, Institut Polytechnique de Paris, Ecole Polytechnique, Palaiseau, France
[7] LPC2E-CNRS-CNES-Orleans University, Orleans, France
[8] Tohoku University, Aoba-ku, Sendai 980-8578, Japan
[9] Institute of Arts and Sciences, Yamagata University, Yamagata 990-0021, Japan
[10] Swedish Institute of Space Physics, Box 812, 98128 Kiruna, Sweden
[11] Keio University, Endo, Fujisawa, 252-0882, Japan

three dimensions at altitudes from several 10 km to several 100 km (Nakamura et al. 2021).

Mass spectrum analyzer (MSA), one of the scientific instruments onboard the MMX spacecraft, consists of an ion energy mass spectrum analyzer and magnetometers. In the vicinity of the Mars-moons system, there are ions emitted from the surface of the Martian moons due to the solar wind sputtering, photon-stimulated desorption and so on (e.g., Madey et al. 1998), and atmospheric ions escaping from Mars due to their interactions with the solar wind. MSA will remotely examine the surface material of the moons and will directly observe the escape of the Martian atmosphere, while monitoring the solar wind, to contribute to the MMX scientific objectives (Yokota et al. 2021). The MSA observations aim to put constraints on models of the origin of the moons, and the evolution of the Martian atmosphere.

The ion analyzer of MSA is composed of an electrostatic energy analyzer and a time-of-flight (TOF) mass spectrometer, which will measure the three-dimensional velocity distribution function and mass distribution of low-energy ions. The main targets of the ion analyzer are solar wind ions of typically ~ 10^8 particles cm^{-2} s^{-1}, those scattered at the Phobos surface, water-related ions of ~ 10^5 ions cm^{-2} s^{-1} generated in the predicted Phobos gas torus, secondary ions of ~ 10^4 ions cm^{-2} s^{-1} sputtered from the Phobos surface, and escaping ions of ~ 10^4- ~ 10^7 ions cm^{-2} s^{-1} from the Martian atmosphere, as summarized in Yokota et al. (2021). Although solar wind ions are dominated by protons and alpha particles (H^+ and He^{++}), the ions emitted from Phobos are expected to range from volatile ions (e.g., Na^+ and K^+) to refractory ions (e.g., Mg^+, Ca^+, and Fe^+) (Schaible et al. 2017; Yokota et al. 2021), like those from the Earth's Moon (Halekas et al. 2015; Yokota et al. 2009; 2014; 2020). Assuming that Phobos originated as a captured asteroid with internal ice, the current water (H_2O) emission was estimated to be ~ 0.3- ~ 3 g/s (Fanale and Salvail 1990). Such H_2O molecules escape the orbit of Phobos and become trapped in a keplerian orbit around Mars (Ip and Banaszkiewicz 1990), resulting in an envelope of all the permitted trajectories, or 'torus' (Krymskii et al. 1992; Mura et al. 2002). The H_2O gas torus may produce a flux of H_2O-related ions (O^+, OH^+, H_2O^+, etc.) (Poppe et al. 2016). In the Martian magnetosphere, it has been reported from Mars Express and Mars Atmosphere and Volatile EvolutioN (MAVEN) observations that the Martian exosphere is composed of thermal and non-thermal populations (Chaffin et al. 2015; Deighan et al. 2015; Rahmati et al. 2015) (followed by the generation of H^+ and O^+ by photoionization, etc.) and that the Martian ionospheric ions (O^+, O_2^+, CO_2^+) are leaking due to non-thermal escape (e.g., Carlsson et al. 2006; Dong et al. 2015; Inui et al. 2018). Although the MAVEN TOF mass spectrometer (McFadden et al. 2015) had limited resolution, minor components (e.g., C^+) were identifiable (e.g., Hanley et al. 2024) and clearly separable using fitting techniques (Picket et al. 2021).

Table 1 Performance and specification of the ion energy mass spectrum analyzer of MSA

Parameter	Value	Notes
Energy range resolution	~ 5 eV/q to ~ 30 keV/q ~ 10%	$\Delta E/E$(FWHM)
FOV range resolution	≥ 2π steradian 22.5° × 11.25° per channel	(FWHM)
g-factor	≥10^{-4} cm^2 sr eV/eV per channel	
Mass range resolution	1–100 amu ~ 100	$m/\Delta m$(FWHM)
Sensor size	ϕ 250 mm × 480 mm	
Sensor mass	5.64 kg	Including HVPS boxes

The ion analyzer of MSA, which we have developed for the MMX mission, is a successor to the high-resolution ion mass analyzers for the Kaguya (Saito et al. 2008a, b; 2010; Yokota et al. 2005) and BepiColombo/Mio (Delcourt et al. 2009; 2016) missions, and will provide unprecedented information on the Phobos surface materials and Martian atmospheric escape by minutely separating the various ion species described above. In this paper, we present the instrumentation and design of the ion analyzer, and summarize the performance obtained from the flight model (FM) calibration tests. A report of the magnetometers of MSA is made in Matsuoka et al. (this issue, under review).

2 Instrumentation and design overview

Based on the MMX scientific objectives (Kuramoto et al. 2021), we estimated the performance requirements for the ion analyzer of MSA as shown in Table 1 (Yokota et al. 2021). Most parameters are standard for space plasma measurements, but the exception is considerably high mass resolution ($m/\Delta m \sim 100$) to separate refractory ions of Phobos origin and Martian atmospheric ions and their key isotopes. Such high mass resolution was achieved by further optimization of the geometry as performed by Gilbert et al. (2010), based on the previously developed ion mass analyzers using the linear-electric-field (LEF) TOF method (e.g., McComas et al. 1990).

Figure 1 shows a photograph and cross section of the FM of the ion analyzer, which is cylindrically symmetric in shape and consists of an energy analyzer and a mass analyzer. The photo shows a component of MSA, which includes the ion analyzer shown in the cross section, and two boxes of high-voltage power supplies (HVPSs)

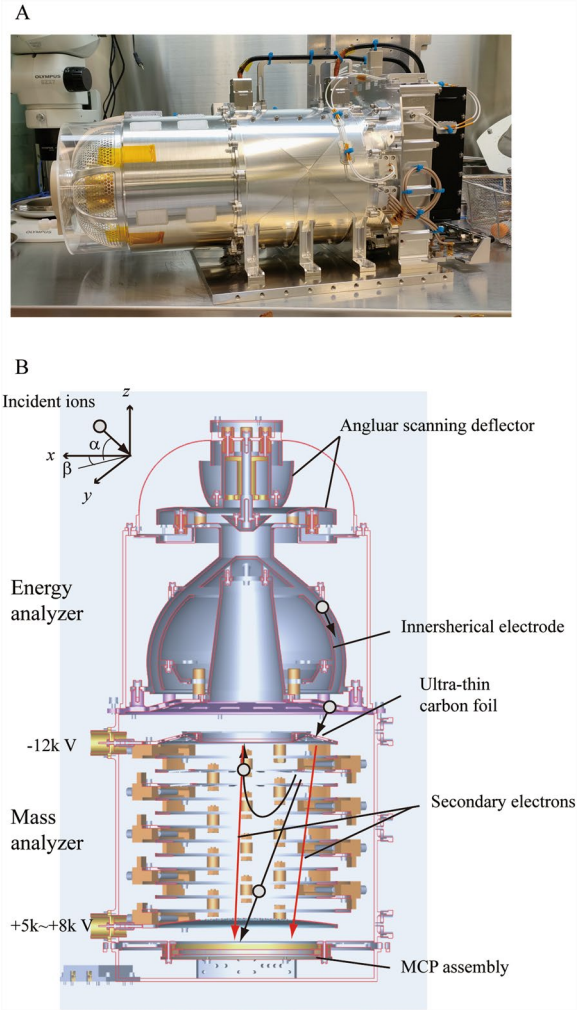

Fig. 1 Photograph (**A**) and cross-sectional view (**B**), of the MSA ion analyzer. Trajectories of incident ions (black) and secondary electrons (red) are illustrated in the cross-sectional view. The analyzer will be covered entirely except for the aperture entrance by multilayer insulation (MLI) when mounted on the spacecraft

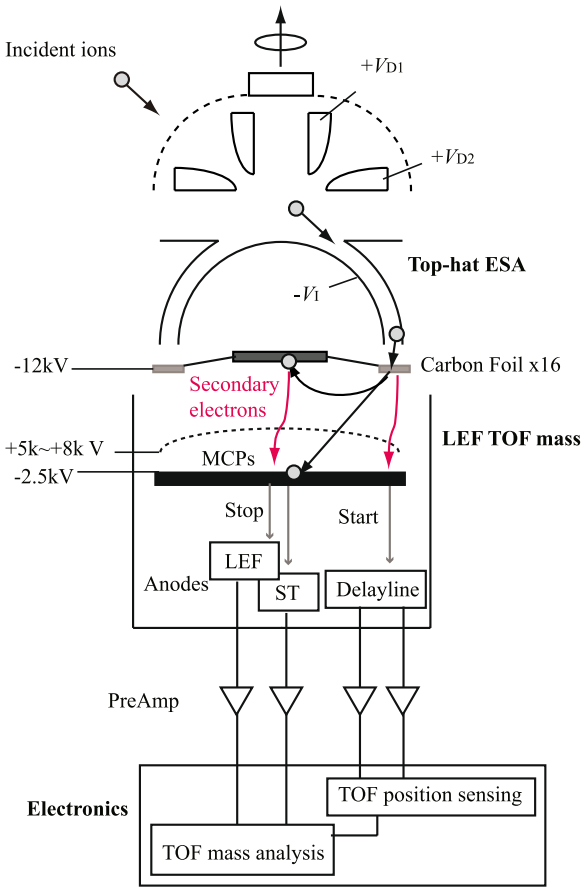

Fig. 2 Block diagram of the MSA ion analyzer functions

connected to the right. The energy analyzer is a top-hat electrostatic analyzer (ESA) using double spherical electrodes for energy/charge (E/q) measurements (e.g., Carlson et al. 1982; Young et al. 1988), and is equipped with a pair of angular scanning deflectors at the 360° entrance aperture for a hemispherical (2π-steradian) field-of-view (FOV) (e.g., Carlson and McFadden 1998; Yokota et al. 2005). Incident ions with the appropriate E/q pass through the ESA and are post-accelerated toward the entrance of the mass analyzer, on which ultra-thin carbon is mounted (see Figs. 1 and 2). The mass analyzer measures the TOF of the incident ions to obtain the mass/charge (m/q). The TOF measurement is performed by using secondary electrons emitted when the incident ions pass through the carbon foil as the start signal, and the incident particles themselves or secondary electrons emitted when incident ions hit the ceiling of the TOF chamber as the stop signal. All of these are detected by a micro-channel plate (MCP) assembly at the bottom, as shown in Fig. 2. In the following, we describe the detail of these key components.

2.1 Spherical ESA

Figure 3 shows the geometry of the ion optics of the ion analyzer. The radii of the inner and outer spherical ESA electrodes are 57.0 mm and 62.0 mm, respectively. In addition, the actual ESA surfaces are serrated and blackened for UV rejection, as shown in Fig. 4A. A negative sweep voltage ($-V_I$) from 0 to − 5 kV is applied to the inner ESA electrode for E/q analysis up to 30 keV/q. The relation is expressed by

$$E/q = k_E V_I, \tag{1}$$

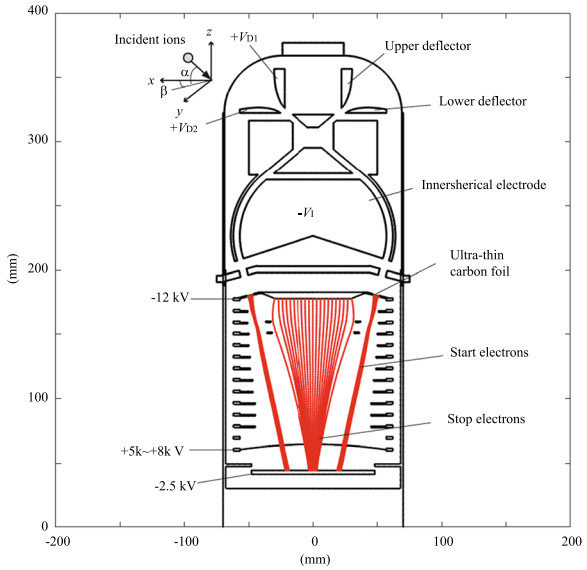

Fig. 3 Ion optics and trajectories of the start/stop electrons (red) attracted to the MCP surface. All applied voltages are also indicated

where $k_E \sim 6$ is the analyzer constant. The waveform of $-V_I$ during observation operation is planned to be a logarithmically stepped sweep.

2.2 Angular scan

The two angular scanning deflectors are alternately applied with a positive sweep high voltage ($+V_{D1}$ or $+V_{D2}$) up to+5 kV to extend the FOV to more than a hemisphere (2π steradian). While the high voltage is applied to one deflector, the other one is grounded. Application of a positive voltage restrains photoelectron emissions from these deflectors when exposed to the sunlight. An electrode with dome-shaped grid structure entirely covers the entrance aperture and deflectors to shut in the electric field generated by $+V_{D1}$ or $+V_{D2}$. It should be noted that although a single grid is used for the ion analyzer, a double grid is more suitable for precise plasma measurements because it suppresses electric field leakage (e.g., Pollock et al. 2016). The actual dome-shaped electrode and deflectors are alodine treated and gold plated, respectively, for thermal properties (see Fig. 4B).

Figure 5 shows a close-up of the dimensions of the angular scanning deflectors. Centered at 40°, the elevation angle (α) of the FOV can be deflected up to $-50°$ or $+50°$ by applying $+V_{D1}$ and $+V_{D2}$, respectively. The deflectors possess a curved surface described by $y = x^{1.7}$ which we found best met the performance requirements. The relation between the appropriate incident angle of α, the deflection voltage (V_D), and E/q, is empirically given by

$$\alpha = k_D \frac{V_D}{E/q} + 40°, \tag{2}$$

$$|V_D| = \begin{cases} V_{D1} (V_D < 0) \\ V_{D2} (V_D > 0), \end{cases} \tag{3}$$

where the sign of V_D indicates whether it is V_{D1} or V_{D2}. In other words, negative (positive) V_D indicates that a positive voltage of $|V_D|$ is applied to the upper (lower) deflector as $V_{D1}(V_{D2})$. The nominal value of k_D is 100° with a slight variation of less than a few degrees over the range of α between $-10°$ and 90°. Probably due to our own rule of spacing between electrodes of 1 mm/kV or more to prevent electrical discharges, a voltage of twice the energy of single-charged incident ions as V_D is required to cover the entire hemispheric FOV, as summarized by Kasahara et al. (2023). As shown in Eqs. 1 and 2, the deflection angle of α is proportional to V_D/V_I. The nominal observation will target ions below 10 keV/q which can be observed in all FOVs at $|V_D| \leq 5$ kV. Depending on the observation situation, the energy range may be expanded to 30 keV/q, while the FOV becomes limited. The FOV limit for the target energy can be obtained from Eq. 2.

2.3 LEF TOF mass analyzer

Figure 4C shows that ultra-thin carbon foil is mounted on 333 lines/inch metal grid defining 16 windows with an azimuthal angle of 22.5°. The TOF measurement requires the carbon foil for secondary electron emission, which is used as the starting signal. However, the carbon foil causes energy loss and angular scattering to the incident ions, increasing the TOF variation and reducing the mass resolution. To reduce the variations in angular scattering and energy loss and increase transmission efficiency, the post-acceleration voltage of -12 kV ($-V_{PA}$) is applied to the carbon foil, as shown in Figs. 1 and 2.

The mass analyzer uses an LEF to minimize the effect of energy and angle variation on the TOF of the incident ions (e.g., McComas et al. 1990). The TOF chamber which holds the LEF is longer than that of the previous analyzers (Yokota et al. 2005; Delcourt et al. 2016) to achieve a high mass resolution, as shown in Fig. 3. Most of the incident ions are neutralized during passage of the carbon foil (e.g., Allegrini et al. 2016) and continue to travel straight until they reach the MCP assembly as a stop signal (see Figs. 1 and 2). In this case, for an incident ion with energy E, the time difference between the start and stop signals yields the conventional straight (ST) TOF (ΔT_{ST}) as shown below,

$$\Delta T_{\mathrm{ST}} = L' \sqrt{\frac{m}{2E'}}, \tag{4}$$

where m, $L\prime$, and $E\prime$ denote the mass, flight length, and energy after the carbon foil transmission of the incident

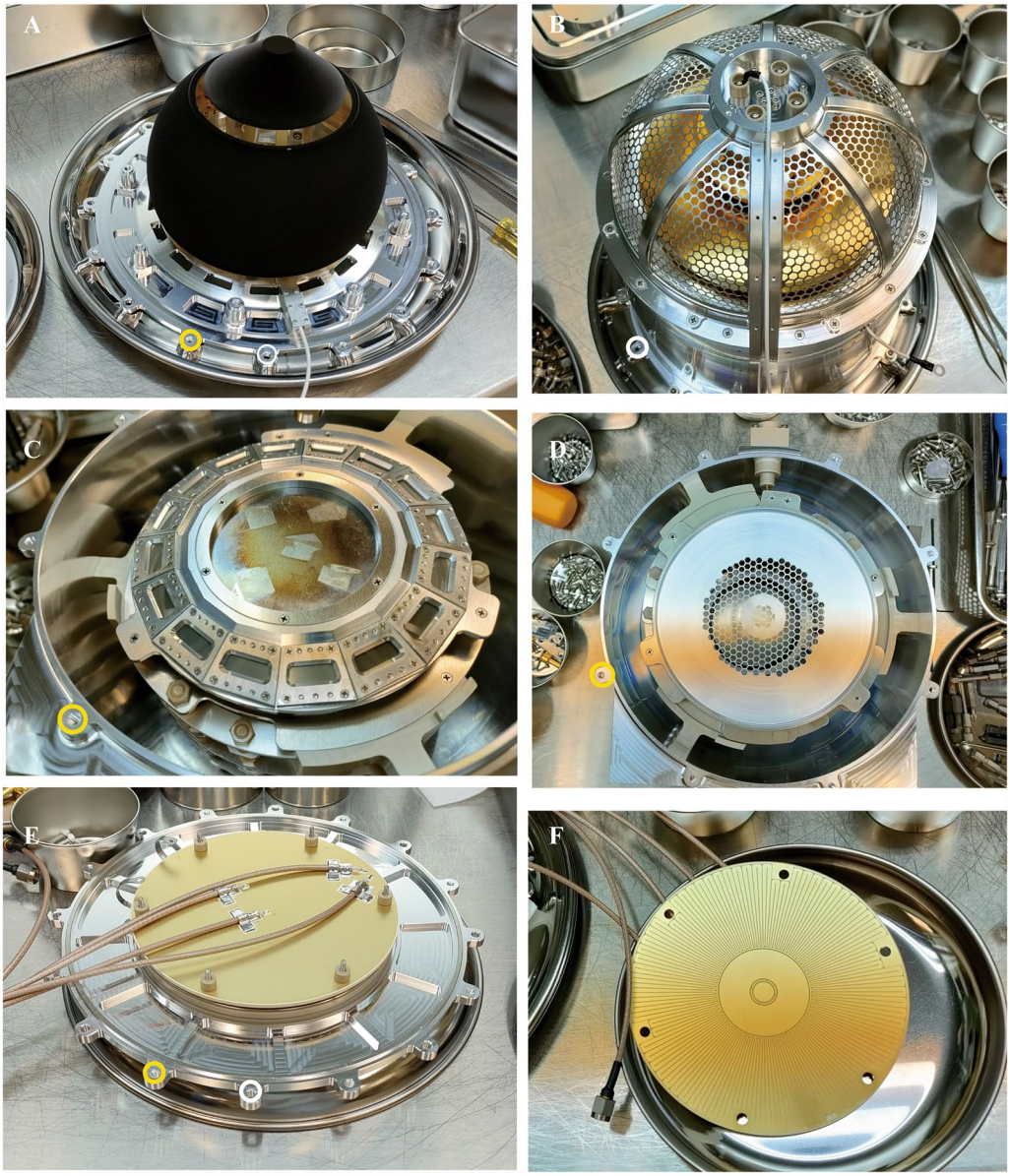

Fig. 4 Photographs of components of the MSA ion analyzer. The inner spherical ESA (**A**), dome-shaped grid electrode over the angular scanning deflectors and aperture entrance (**B**), Ultra-thin carbon foil mounted on 16 holders (**C**), reflection grid electrode of the TOF chamber (**D**), MCP assembly (**E**), and anode board which contains a delay line anode, and ST and LEF stop anodes (**F**). Tapped holes and through holes for 3-mm screws are indicated by yellow and white circles, respectively

ion, respectively. As Eq. 4 shows, ΔT_{ST} is affected not only by m but also by dispersion of the energy loss $(E + qV_{PA} - E\prime)$ (e.g., Asamura et al. 2018; Yokota et al. 2017), which limits the improvement in mass resolution. Moreover, angular scattering changes $L\prime$.

In a minority case, the incident ions pass through the carbon foil as positive ions and are reflected by the LEF, causing secondary electron emission from the ceiling of the TOF chamber. The secondary electrons are detected as a stop signal. Since the motion of ions reflected by the LEF is given by the equation of the simple harmonic motion, the LEF TOF (ΔT_{LEF}) depends only on the mass as follows,

$$\Delta T_{\mathrm{LEF}} = \pi \sqrt{\frac{m}{qC_0}}, \tag{5}$$

where C_0 is a constant that is determined solely by the electromechanical configuration of the TOF chamber.

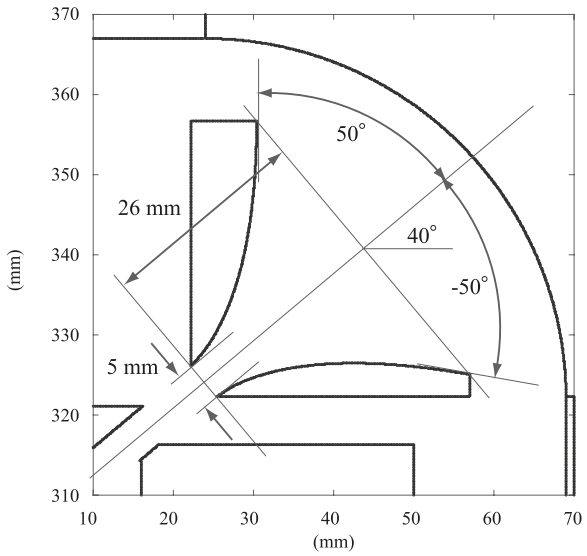

Fig. 5 Dimensions of the angular scanning deflectors

reflect the incident ions, a grid electrode applied with +5 ~+8 kV ($+V_{REF}$) is installed at the bottom (see Figs. 1 and 2). Figure 6 shows a close-up of the electric potential and reflected ion trajectories in the TOF chamber. Contour lines linearly divide the potential into 20 levels. The trajectories were calculated for 20 oxygen ions (O^+) with an initial energy of 4 keV passing through a point on the carbon foil at $+V_{REF} = +5$ kV.

In the case that incident ions are converted to negative ions by the carbon foil, the detection of stop signals is similar to that for neutral particles. Since $+V_{\mathrm{REF}}$ accelerates the negative ions, the TOF is smaller than ΔT_{LEF}.

The LEF in the TOF chamber ensures a clearance between the detection areas of start and stop electrons on the MCP surface, as shown in Fig. 3. The grid electrodes are masked in a doughnut shape, as shown in Fig. 4D, to prevent the neutralized incident ions from reaching the narrow central region where the stop electrons arrive. The central region is dedicated to the LEF TOF measurement.

The ceiling is an MgO-coated copper beryllium plate to improve the efficiency of the stop electron emission. To

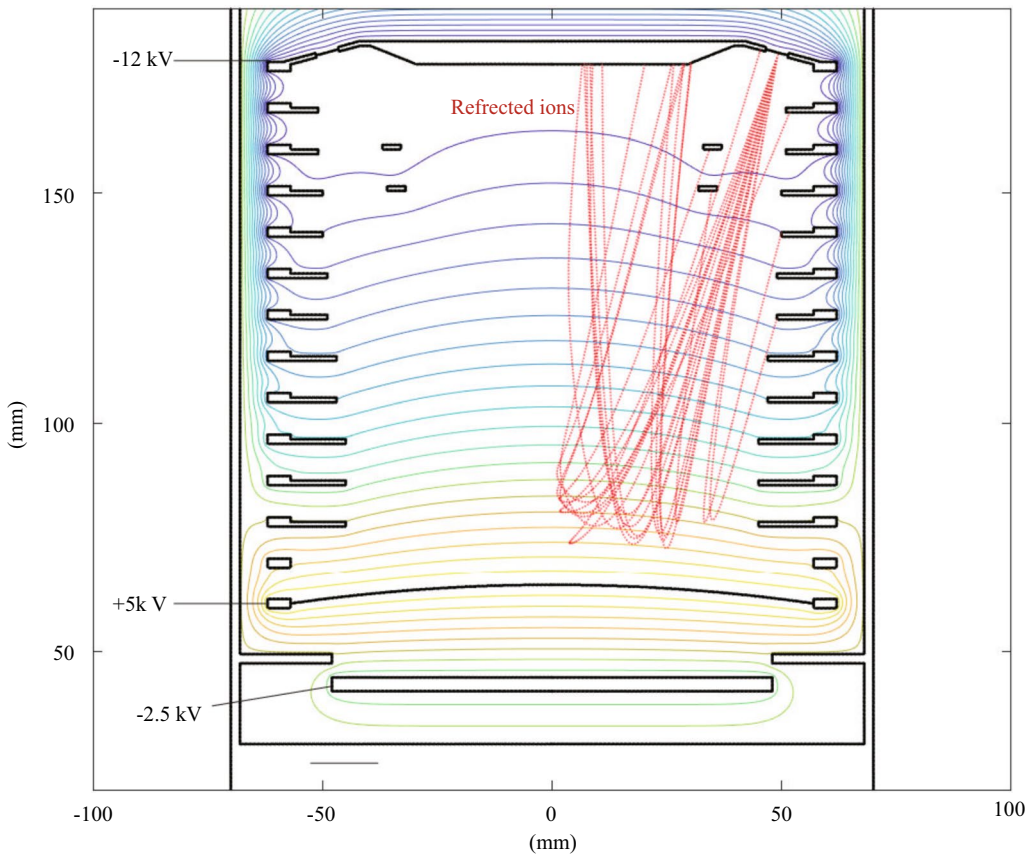

Fig. 6 Electric potential and reflected ion trajectories (red) in the TOF chamber. All applied voltages are also indicated. Contour lines linearly divide the potential into 20 levels. The trajectories were calculated for 20 oxygen ions (O^+) with an initial energy of 4 keV passing through a point on the carbon foil

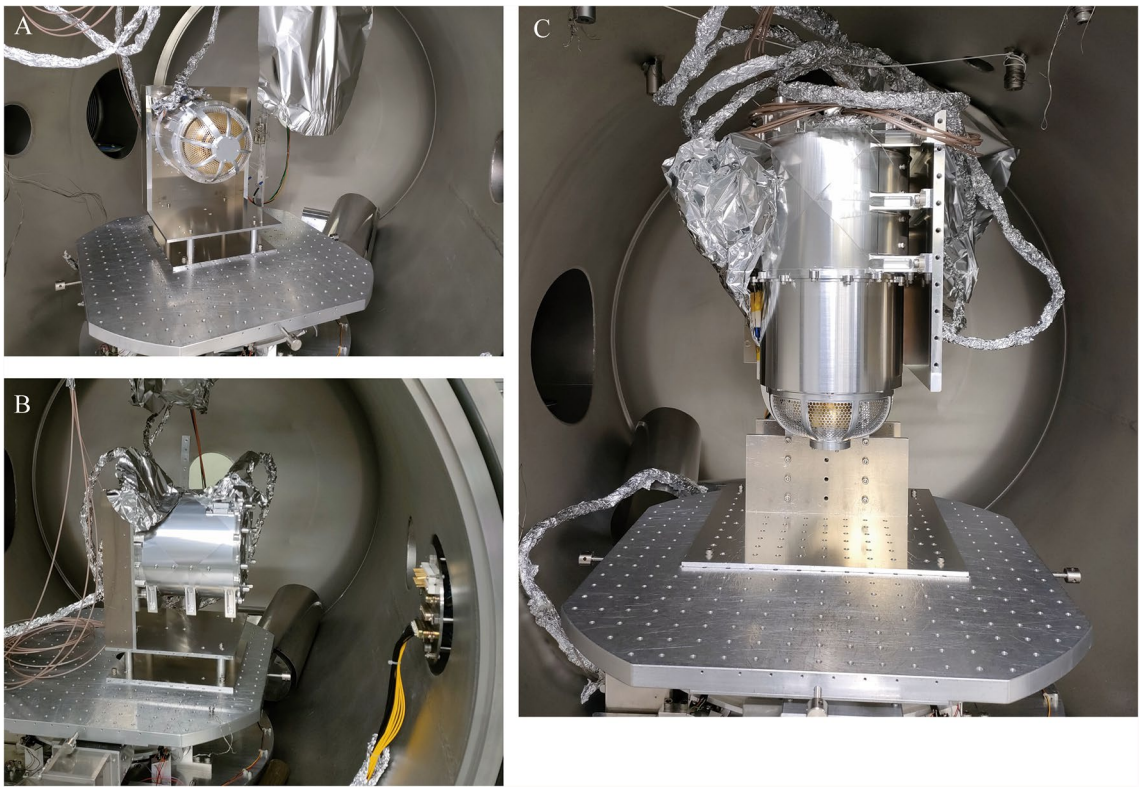

Fig. 7 Photographs of the MSA ion analyzer in a vacuum chamber for performance tests. Ion energy analyzer (**A**), ion mass analyzer (**B**) and MSA ion analyzer combining the two (**C**)

2.4 Detector

Figure 4E shows the MCP assembly which consists of three MCP plates in the z-stack configuration and an anode board. On the anode board, there is an outermost circular, zigzag delay line anode for the start signals and two circular anodes in the center for the stop signals of the ST and LEF TOF measurements (see Fig. 4F). As shown in Fig. 2, the delay line anode also performs 360° azimuthal position sensing by detecting the start electrons and measuring the difference in arrival time from both sides to divide the 360° azimuthal angle (β) of the ion incidence into 16 channels (Saito et al. 2017). The LEF stop anode is placed in the center of the board to match the size of the detection area of the converging stop electrons. The ST stop anode is located between the LEF stop anode and the delay line anode in a donut shape. The two start signals from the delay line anode, and ST and LEF stop signals are transmitted to the electronics with TOF resolution within 1 ns.

3 Analyzer performance

After designing and fabricating the FM of the MSA ion analyzer, we carried out a series of performance tests for calibration data. Performance calculations during design were conducted using an electrostatic field modeling program that has accurately predicted the response of several space plasma analyzers for the MMS (Pollock et al. 2016), Kaguya (Saito et al. 2010; Yokota et al. 2005), and Bepi-Colombo/Mio missions (Delcourt et al. 2009; 2016), and SS520-3 rocket experiment (Yokota et al. 2024). The performance tests were conducted in the Institute of Space and Astronautical Science (ISAS) beam chamber, which was used for the previous analyzers. To test the characteristics of the energy analysis, the analyzer must be oriented in all directions relative to the ion beam. However, there is not enough space in the ISAS chamber and no gimbals to hold and widely rotate the entire analyzer, as shown in Figs. 7A and 7B. Therefore, detailed testing was performed separately on the ion energy and mass analyzers. Although the beam direction was limited, beam tests were also performed for all channels in the entire combination of the two analyzers to check the efficiency, as shown in Fig. 7C.

The ion source in the ISAS facility which we utilized is capable of stably supplying ion beams from 2 to 10 keV. Neutral gas entering from a gas reservoir is ionized by filament's thermal electrons. The reservoir was filled with a mixture of H_2, N_2, and CO_2 for the tests. The ionized

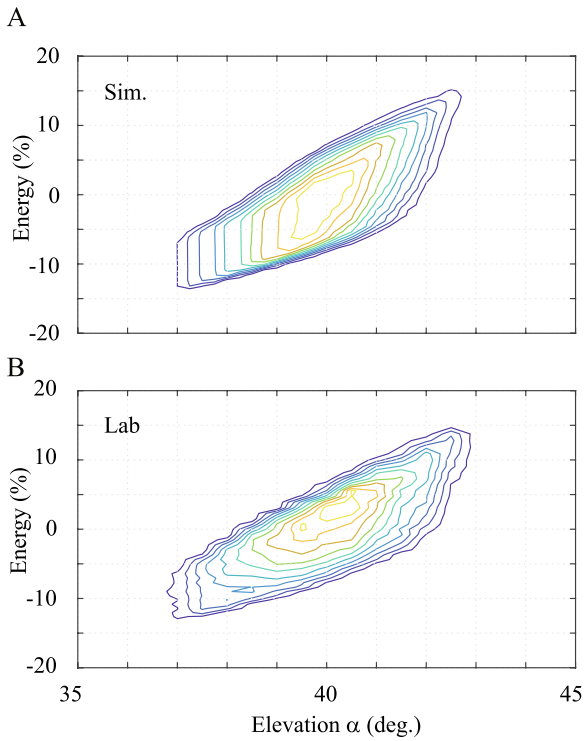

Fig. 8 Energy-elevation responses of the ion energy analyzer. The responses were calculated in the model (**A**) and measured in the laboratory (**B**). Contour lines linearly divide the sensitivity of the peak transmission into ten levels

gas is accelerated, mass/charge-selected by the electric and magnetic field velocity filter, and ejected as ion beam whose energy is well-defined. The stability of the ion beam is continuously checked by monitoring it with an ammeter connected to a grid electrode installed in the beam passage, but the absolute flux is indefinite. No geomagnetic shielding such as a Helmholtz coil is implemented for the ion beam. In the following, we show the results of the performance tests and evaluate them by comparing the calculated and measured characteristics.

3.1 Ion energy analyzer

To measure the characteristics of the ion energy analyzer, we used a 4 keV N^+ ion beam whose energy was well-defined with uniform intensity over the aperture of the analyzer. Figure 8 shows energy-elevation (α) responses calculated in the numerical model (Panel A) and measured in the laboratory (Panel B) for channel 0. In the numerical model, the detection is that the incident ions reach the carbon foil, and the direction of incidence is within 3 degrees of the normal direction of the carbon foil. Contour lines linearly divide the sensitivity of the peak transmission into ten levels. The responses were obtained under the condition that the upper and lower deflectors were grounded. The performances of the FM measured in the laboratory are consistent with that in the model, with an energy resolution of $\sim$ 10% and an angular resolution of less than 11.25° (see Table 1). The analyzer constant k_E obtained in the performance test was 6.1, slightly smaller than that in the model, 6.3. This is because the spherical ESA surfaces were serrated for UV rejection, and thus the actual gap is wider than 5 mm in the model.

To demonstrate the performance of the angular scanning, Fig. 9 shows energy-elevation responses with 16 different V_D/V_I (V_{D1}/V_I or V_{D2}/V_I) calculated in the model (Panel A) and measured in the laboratory (Panel B) for channel 0. The responses at $V_D/V_I = 0$ ($V_{D1} = 0$ and $V_{D2} = 0$) are the same as those in Fig. 8. All measured responses also achieve an energy resolution of $\sim$ 10% and an angular resolution of less than 11.25°, similar to those of the model. Because the angular scanning deflectors are gold plated, the dimensions are not exactly the same as those in the model. Although there are differences up to a few degrees in the angular distribution between the responses obtained from the model and the tests depending on the deflection angle, they are in good agreement overall. By applying up to three times the voltage of V_I to V_D (V_{D1} or V_{D2}), the elevation angle is covered in the range of ±50° centered at 40°. The 16 different V_D/V_I are also needed to fill the elevation range of ±50° without gaps. In future actual observation operation, such 16 different deflector voltages will be applied for each V_I. This elevation range and 3600° aperture allows the ion energy analyzer to have more than a hemispheric (2 π sr) FOV. Since the maximum output of the HVPSs for V_{D1} and V_{D2} is 5 kV, the incident ions that can be deflected by ±50° are limited to $<\sim$ 10 keV/q.

Similar beam tests were performed on all 16 channels to generate pre-flight calibration data. As a summary of the ion energy analyzer performance, Fig. 10 shows the analyzer sensitivity (g-factor) (Panel A), the average elevation (α) (Panel B), and the average energy/charge per ESA voltage ($E/qV_I = k_E$) (Panel C) for 16 channels (colored dots) compared to those calculated in the model (solid lines). The analyzer sensitivity was designed not to change significantly with respect to deflection angle, as indicated by the model results, and the same trend was obtained in the performance test results. There is a difference of a few factors between the analyzer sensitivities obtained in the tests and the model depending on the deflection angle and channel. The characteristics obtained in the tests, not just the sensitivity, are affected by differences in the surface serrations, treatments and coatings in each electrode and the efficiency of the MCP-based detector, which are not included in the model. In

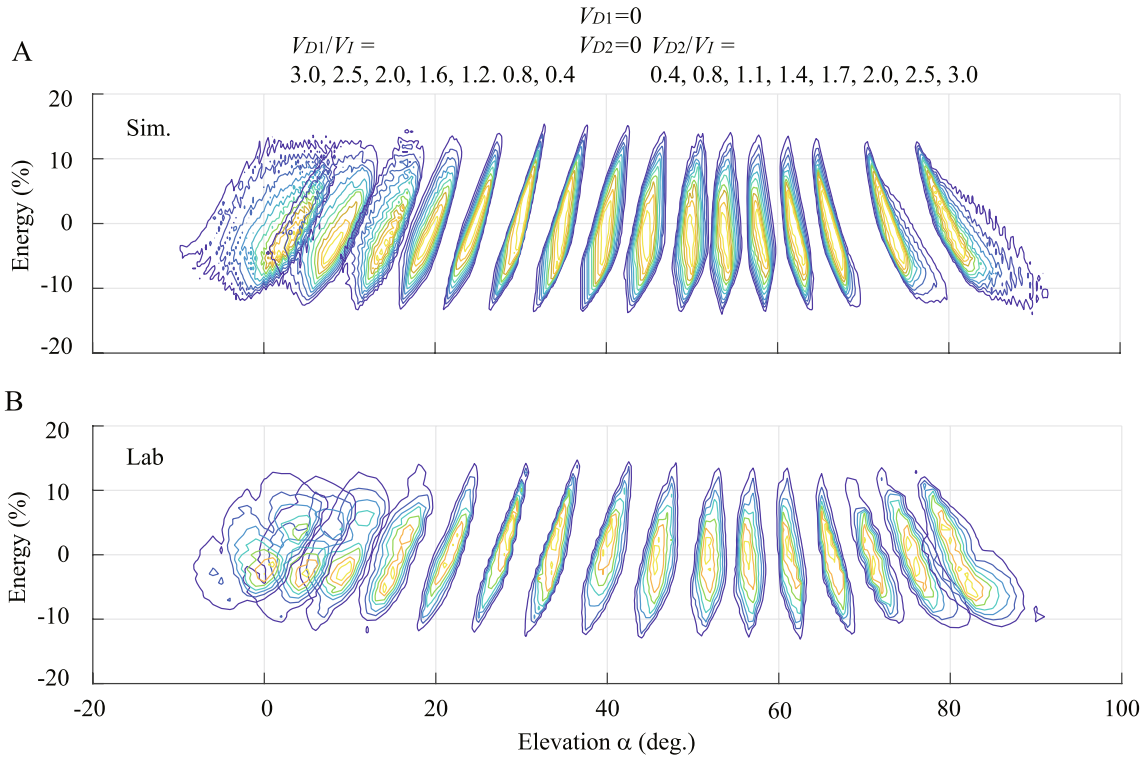

Fig. 9 Energy-elevation responses of the ion energy analyzer for 16 deflection angles. The responses with 16 different V_D/V_I (V_{D1}/V_I or V_{D2}/V_I) are calculated in the model (**A**) and measured in the laboratory for channel 0 (**B**). Contour lines linearly divide the sensitivity of the peak transmission into ten levels

the case of the sensitivity, the efficiency of the MCP-based detector is considered to be particularly influential.

The average elevation angles for all channels range from − 10 to +90°, with relatively few differences between channels, consistent with the design values indicated by the model. This result also supports that the ion analyzer has a hemispheric (2π sr) FOV. The analyzer constant $k_E \sim 6.1$ was obtained in the performance tests with relatively little variation at all deflection angles and channels. Since the FM will perform velocity moments (VMs) calculations in the onboard software, these characteristics are organized and used as look-up tables.

3.2 Ion mass analyzer

The ion mass analyzer was also examined for all 16 channels using several types of ion beams in the laboratory. Figure 11 shows the ST TOF profiles (ΔT_{ST}) using signals from the ST stop anode, which were generated by incident ions neutralized during the carbon foil transmission. For these TOF profile measurements, we utilized a mass/charge-filtered 4 keV ion beam for each ion species, and all the TOF measurements were taken until the start signals were detected 100,000 times. It should be noted that since negative ions are attracted to the delay line anode like the start electrons, their TOF slightly appears in the TOF measurements using the ST anode. The neutralized particles fly straight from the carbon foil to the MCP surface in a 13 cm path, unaffected by the LEF in the TOF chamber. The ST TOF profiles of all 16 channels are in good agreement with each other and with that calculated in the model assuming a foil thickness of 5 nm. Carbon foils labeled 0.5 μg/cm2 thickness (equivalent to $\sim$ 2.5 nm thickness) were placed on all 16 channel holders, and while the actual thicknesses were all about twice as thick, the variation is not enough to cause significant changes in the TOF profiles from channel to channel. The measured profiles are wider than the calculated ones because there are delays in actual measurements, such as signal processing, that are not included in the model. The mass resolution of the ST TOF mass analysis is estimated to be $m/\Delta m \sim 10$.

Figure 12 demonstrates the high mass resolution of $m/\Delta m \sim 100$, which has been achieved by the LEF TOF technique. The LEF TOF profiles (ΔT_{LEF}) were measured using signals from the LEF stop anode. The measured LEF TOF profiles for 16 channels, which agree with that calculated in the model with small variation, is proportional to $\sqrt{m}$, as shown in Eq. 5. The mass analyzer was manufactured based on a geometry that achieves $m/\Delta m \sim 400$ in the model, but the resolution was

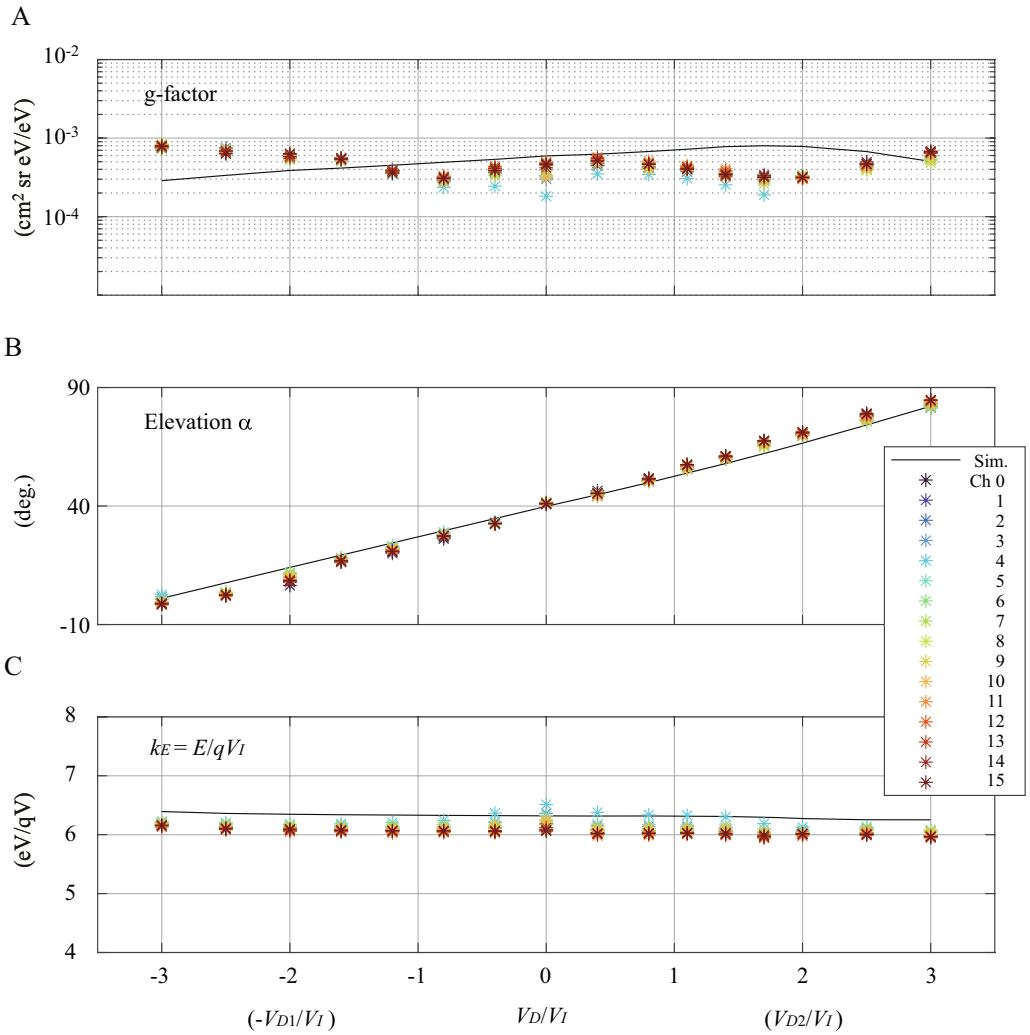

Fig. 10 Characteristics of the ion energy analyzer. Sensitivities (g-factors) (**A**), average elevation (α) (**B**), and average energy/charge per ESA voltage (analyzer constant k_E) (**C**), were calculated in the model (solid line) and measured in the laboratory for all 16 channels (colored dots). The horizontal axis shows the voltage ratio described as V_{D1}/V_I or V_{D2}/V_I. A negative (positive) voltage ratio denotes $V_{D1}(V_{D2})/V_I$ and $V_{D2}(V_{D1}) = 0$

degraded possibly due to signal processing and manufacturing errors. However, this resolution satisfies the performance requirements (see Table 1), and the analyzer is expected to distinguish between metallic elements coming from the Phobos surface in future observations.

4 Discussion

The pre-flight performance tests for the FM calibration data have demonstrated that all the performances shown in Table 1 have been achieved. We confirmed that the ion energy mass spectrum analyzer is capable of measuring a three-dimensional distribution function at least below 10 keV/q and performing mass spectrometry with considerably high resolution. We also measured the overall characteristics of the MSA ion analyzer consisting of the ion energy and mass analyzers, which were quite close to that measured when the two analyzers were separated.

Since the MMX spacecraft is three-axis controlled, the ion sensor scans more than 90° of elevation angle (α) by the angular scanning deflectors and performs position sensing over a 360° azimuth angle (β) divided into 16 channels to acquire a hemispheric FOV. We confirmed that the characteristics of the FM are relatively uniform for all α and for all β. The TOF characteristics also showed no significant variation among channels.

The onboard software of MSA calculates the VMs using the characteristics such as g-factor, k_E, α, β and so on. It also formats the telemetry data and reduces the quantity of data by adding, selecting, or

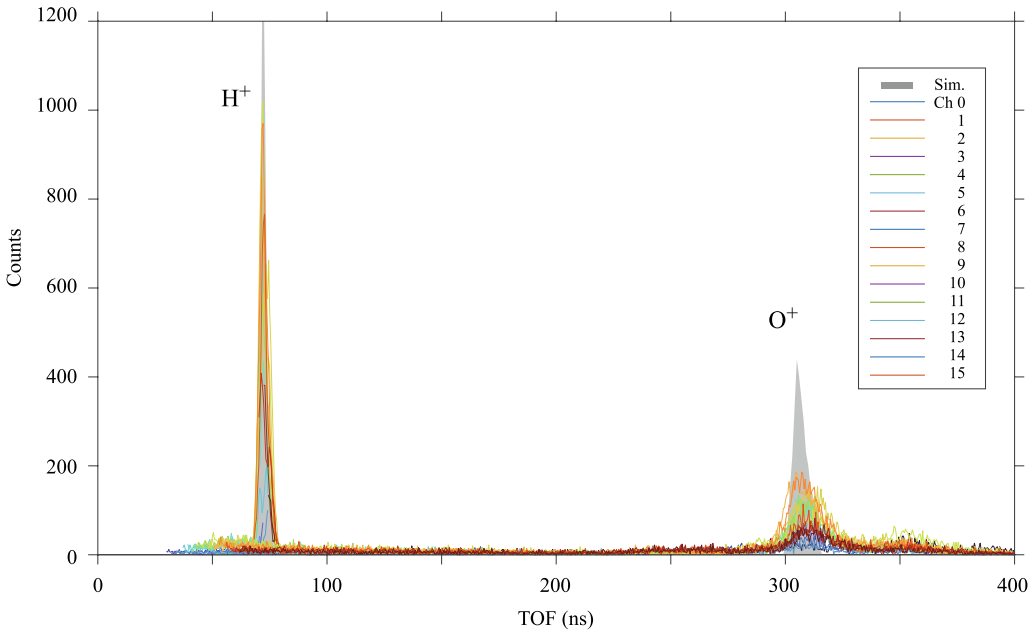

Fig. 11 ST TOF profiles of the ion mass analyzer. The profiles were calculated in the model (gray shades) and measured using stop signals from the ST stop anode in the laboratory for all 16 channels (colored lines)

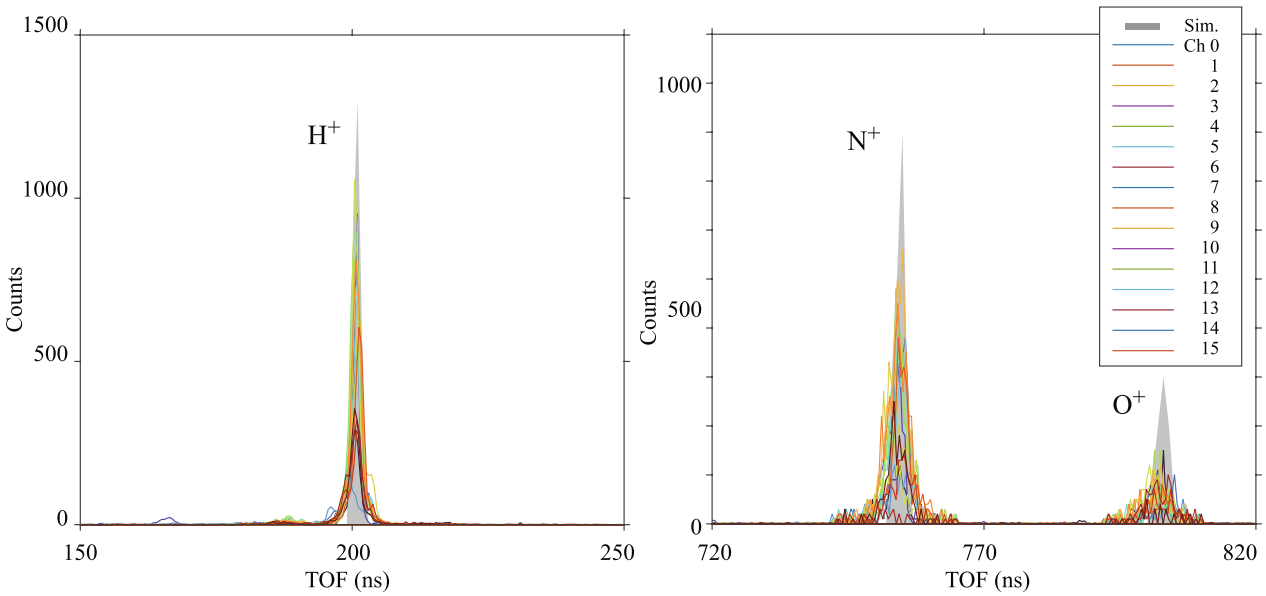

Fig. 12 LEF TOF profiles of the ion mass analyzer. The profiles were calculated in the model (gray shades) and measured using stop signals from the LEF stop anode in the laboratory for all 16 channels (colored lines)

compressing the data. In addition to VMs, the data products include energy spectra, three-dimensional distributions for all ion species and O^+, and ST and LEF TOF-energy distributions at 1 ~ 10-min resolution. The distribution for O^+ is derived using the onboard TOF-energy table.

5 Summary

After the development of the engineering model (EM) of MSA, and Critical Design Review (CDR) held in 2022, we had the Post-Qualification Review (PQR) and Pre-Shipping Review (PSR) which confirmed the completion of the development for the FM of MSA in August 2024. The performance tests and pre-flight calibration presented here were conducted from the end of 2022 to the beginning of 2024. The FM of MSA was handed over to the MMX spacecraft system. The FM of MSA was integrated into the spacecraft exploration module, and the pre-flight test of the spacecraft system has started.

After the launch and arrival at Mars scheduled in 2026 and 2027, respectively, the ion analyzer of MSA will perform in situ observations of ions which are related with the surface and tori of the Martian moons, Martian atmosphere, and the solar wind together with the magnetometers of MSA to address the MMX mission goals. In the past we have succeeded in mass spectrometry of ions around the Earth's Moon and obtained many scientific results, such as the solar wind ions scattered at the lunar surface (Saito et al. 2008b), secondary ions emitted from the surface (e.g., Yokota et al. 2009; Tanaka et al. 2009), escaping ions from the Earth's atmosphere (Terada et al. 2017), etc. Similar observations will be made around the Martian moons, but with much improved mass resolution.

Abbreviations

EM	Engineering model
ESA	ElectroStatic analyzer
FM	Flight model
FOV	Field-of-view
FWHM	Full width at half maximum
HVPS	High-voltage power supply
ISAS	Institute of Space and Astronautical Science
JAXA	Japan Aerospace Exploration Agency
LEF	Linear-electric-field
MAVEN	Mars Atmosphere and Volatile EvolutioN
MCP	Micro-channel plate
MMX	Martian Moons eXploration
MSA	Mass spectrum analyzer
ST	Straight
TOF	Time-of-flight

Acknowledgements

The authors would like to express sincere thanks to all members of the MMX mission. The authors would like to thank Prof. T. Mukai, Prof. H. Hayakawa, and Dr. T. Goka for helpful comments. The MSA experiment was manufactured by Meisei Electric Co., Ltd. The ion optics was machined by YS design. This study was supported by ISAS/JAXA as a collaborative program with the Space Chamber Laboratory and the joint research program of the Institute for Space–Earth Environmental Research (ISEE), Nagoya University.

Author contributions

SY wrote the manuscript. SY, AM, NM, YS, KA, SK, DD, LZH, and YK contributed to the development of the experiment. NT, KK, YH, HN, KM, SS, YF, SI, KS, and MNN contributed to consideration of the observation objectives. All authors read and approved the final manuscript.

Funding

The MSA instrumentation is funded by the Japan Aerospace Exploration Agency (JAXA). This work was partly supported by JSPS KAKENHI Grant Number 24K00693, 20K04039, 22H00164, 21H04509, and 17H01164.

Availability of data and materials

The datasets used and/or analyzed during the current study are available from the corresponding author on reasonable request.

Declarations

Competing interests

The authors declare that they have no competing interest.

Received: 28 October 2024 Accepted: 31 May 2025
Published online: 11 July 2025

References

Allegrini F, Ebert RW, Funsten HO (2016) Carbon foils for space plasma instrumentation. J Geophys Res Space Phys 121:3931–3950. https://doi.org/10.1002/2016JA022570

Asamura K, Kazama Y, Yokota S, Kasahara S, Miyoshi Y (2018) Low-energy particle experiments—ion analyzer (LEPi) onboard the ERG (Arase) satellite. Earth Planets Space 70:70. https://doi.org/10.1186/s40623-018-0846-0

Barruci MA, Reess JM, Bernardi P, Doressoundiram A, Fornaiser S, Du ML, Iwata T, Nakagawa H, Nakamura T, Andre Y, Aoki S, Arai T, Baldit E, Beck P, Buey JT, Canalias E, Castelnau M, Charnoz S, Chaussidon M, Chapron F, Ciarletti V, Delbo M, Dubois B, Gauffre S, Gautier T, Genda H, Hassen-Khodja R, Hervet G, Hyodo R, Imbert C, Imamura T, Jorda L, Kameda S, Kouach D, Kouyama T, Kuroda T, Kurokawa H, Lapaw L, Lasue J, Deit LL, Ledot A, Leyrat C, Ruyet BL, Matsuoka M, Merlin F, Miyamoto H, Moynier F, Tuong NN, Ogohara K, Osawa T, Parisot J, Pistre L, Quertier B, Raymond S, Rocard F, Sakanoi T, Sato TM, Sawyer E, Tache F, Tremolieres S, Tsuchiya F, Vernazza P, Zeganadin D (2021) MIRS an imaging spectrometer for the MMX mission. Earth Planets Space 73:211. https://doi.org/10.1186/s40623-021-01423-2

Carlson CW, Curtis DW, Paschmann G, Michel W (1982) An instrument for rapidly measuring plasma distribution functions with high resolution. Adv Sp Res 2(7):67–70

Carlson CW, McFadden JP (1998) Design and application of imaging plasma instruments. In: Pfaff RF, Borovsky J, Young DT (eds) Measurement techniques in space plasmas particles. American Geophysical Union, Washington

Carlsson E, Fedorov A, Barabash S, Budnik E, Grigoriev A, Gunell H, Nilsson H, Sauvaud J-A, Lundin R, Futaana Y, Holmström M, Andersson H, Yamauchi M, Winningham JD, Frahm RA, Sharber JR, Scherrer J, Coates AJ, Linder DR, Kataria DO, Kallio E, Koskinen H, Säles T, Riihelä P, Schmidt W, Kozyra J, Luhmann J, Roelof E, Williams D, Livi S, Curtis CC, Hsieh KC, Sandel BR, Grande M, Carter M, Thocaven J-J, McKenna-Lawler S, Orsini S, Cerulli-Irelli R, Maggi M, Wurz P, Bochsler P, Krupp N, Woch J, Fränz M, Asamura K, Dierker C (2006) Mass composition of the escaping plasma at Mars. Icarus 182(2):320–328. https://doi.org/10.1016/j.icarus.2005.09.020

Chaffin MS, Chaufray JY, Deighan J, Schneider NM, McClintock WE, Stewart AIF, Thiemann E, Clarke JT, Holsclaw GM, Jain SK et al (2015) Three-dimensional structure in the Mars H corona revealed by IUVS on MAVEN. Geophys Res Lett 42:9001–9008. https://doi.org/10.1002/2015GL065287

Cho Y, Bottger U, Rull F, Belenguer T, Borner A, Buder M, Bunduki Y, Dietz E, Hagelschuer T, Hubers H-W, Kameda S, Kopp E, Lieder M, Lopez G, Moral Inza A, Paproth C, Perez Canora C, Pertenais M, Peter G, Prieto Ballesteros O, Rockstein S, Rodd-Routley S, Rodriguez Perez P, Ryan C, Santamaria P, Sauberlich T, Schrandt F, Schroder S, Stangarone C, Ulamec S, Usui T, Weber I, Westerdorff K, Kuramoto K (2021) In-situ science on Phobos with the Raman spectrometer for MMX (RAX): preliminary design and feasibility of Raman measurements. Earth Planets Space 73:232. https://doi.org/10.1186/s40623-021-01496-z

Deighan J, Chaffin MS, Chaufray JY, Stewart AIF, Schneider NM, Jain SK, A. Crismani SM, McClintock WE, Clarke JT, Holsclaw GM, Montmessin F, Eparvier FG, Thiemann EMB, Chamberlin PC, Jakosky BM, (2015) MAVEN IUVS

observation of the hot corona at Mars. Geophys Res Lett 42:9009–9014. https://doi.org/10.1002/2015GL065487
Delcourt D, Saito Y, Illiano J-M, Krupp N, Berthelier J-J, Fontaine D, Fraenz M, Leblanc F, Fischer H, Yokota S, Michalik H, Godefroy M, Saint-Jacques E, Techer J-D, Fiethe B, Covinhes J, Gastou J, Attia D (2009) The mass spectrum analyzer (MSA) onboard BEPI COLOMBO MMO: scientific objectives and prototype results. Adv Space Res 43:869–874. https://doi.org/10.1016/j.asr.2008.12.002
Delcourt D, Saito Y, Leblanc F, Verdeil C, Yokota S, Fraenz M, Fischer H, Fiethe B, Katra B, Fontaine D, Illiano J-M, Berthelier J-J, Krupp N, Buhrke U, Bubenhagen F, Michalik H (2016) The mass spectrum analyzer (MSA) on board the Bepi-Colombo MMO. J Geophys Res Space Phys 121(7):6749–6762. https://doi.org/10.1002/2016JA022380
Dong Y, Fang X, Brain DA, McFadden JP, Halekas JS, Connerney JE, Curry SM, Harada Y, Luhmann JG, Jakosky BM (2015) Strong plume fluxes at Mars observed by MAVEN: an important planetary ion escape channel. Geophy Res Lett 42(21):8942–8950. https://doi.org/10.1002/2015GL065346
Fanale FP, Salvail JR (1990) Evolution of the water regime of Phobos. Icarus 88(2):380–395. https://doi.org/10.1016/0019-1035(90)90089-R
Gilbert JA, Lundgren RA, Panning MH, Rogacki S, Zurbuchen TH (2010) An optimized three-dimensional linear-electric-field time-of-flight analyzer. Rev Sci Instrum 81(5):053302. https://doi.org/10.1063/1.3429941
Halekas JS, Benna M, Mahaffy PR, Elphic RC, Poppe AR, Delory CT (2015) Detections of lunar exospheric ions by the LADEE neutral mass spectrometer. Geophys Res Lett 42:5162–5169. https://doi.org/10.1002/2015GL064746
Hanley KG, Mitchell DL, Lillis R, Fowler CM, McFadden JP, Jolitz R et al (2024) Space weather induces changes in the composition of atmospheric escape at Mars. Geophys Res Lett 51:e2024GL111676. https://doi.org/10.1029/2024GL111676
Inui S, Seki K, Namekawa T, Sakai S, Brain DA, Hara T, McFadden JP, Halekas JS, Mitchell DL, Mazelle C, DiBraccio GA, Jakosky BM (2018) Cold dense ion outflow observed in the Martian-induced magnetotail by MAVEN. Geophys Res Lett 45:5283–5289. https://doi.org/10.1029/2018GL077584
Ip WH, Banaszkiewicz M (1990) On the dust/gas tori of Phobos and Deimos Geophys. Res Lett 17:857–860. https://doi.org/10.1029/GL017i006p00857
Kameda S, Ozaki M, Enya K, Fuse R, Kouyama T, Sakatani N, Suzuki H, Osada N, Kato H, Miyamoto H, Yamazaki A, Nakamura T, Okamoto T, Ishimaru T, Hong P, Ishibashi K, Takashima T, Ishigami R, Kuo CL, Abe S, Goda Y, Murao H, Fujishima S, Aoyama T, Hagiwara K, Mizumoto S, Tanaka N, Murakami K, Matsumoto M, Tanaka K, Sakuta H (2021) Design of telescopic nadir imager for geomorphology (TENGOO) and observation of surface reflectance by optical Chromatic imager (OROCHI) for the MMX mission. Earth Planets Space 73:218. https://doi.org/10.1186/s40623-021-01462-9
Kasahara S, Tao R, Yoshida E, Yokota S (2023) A two-stage deflection system for the extension of the energy coverage in space plasma three-dimensional measurements. Earth Planets Space 75:91. https://doi.org/10.1186/s40623-023-01845-0
Kobayashi M, Krüger H, Senshu H, Wada K, Okudaira O, Sasaki S, Kimura H (2018) In situ observations of dust particles in Martian dust belts using a large-sensitive-area dust sensor. Planet Space Sci 156:41–46. https://doi.org/10.1016/j.pss.2017.12.011
Krymskii AM, Breus TK, Dougherty MK, Southwood DJ, Axford WI (1992) The electromagnetic effects of the solar wind interaction with the Phobos neutral gas halo and dust torus. Planet Space Sci. https://doi.org/10.1016/0032-0633(92)90032-J
Kuramoto K, Kawakatsu Y, Fujimoto M, Araya A, Barucci MA, Genda H, Hirata N, Ikeda H, Imamura T, Helbert J, Kameda S, Kobayashi M, Kusano H, Lawrence DJ, Matsumoto K, Michel P, Miyamoto H, Morota T, Nakagawa H, Nakamura T, Ogawa K, Otake H, Ozaki M, Russell S, Sasaki S, Sawada H, Senshu H, Tachibana S, Terada N, Ulamec S, Usui T, Wada K, Watanabe S, Yokota S (2021) Martian moons exploration MMX: sample return mission to Phobos elucidating formation processes of habitable planets. Earth Planets Space. https://doi.org/10.1186/s40623-021-01545-7
Lawrence DJ, Peplowski PN, Beck AW, Burks MT, Chabot NL, Cully MJ, Elphic RC, Ernst CM, Fix S, Goldsten JO, Hoffer EM, Kusano H, Murchie SL, Schratz BC, Usui T, Yokley ZW (2019) Measuring the elemental composition of phobos: the mars-moon exploration with GAmma rays and NEutrons (MEGANE) investigation for the Martian Moons eXploration (MMX) Mission. Earth Space Sci 6:2605–2623
Madey TE, Yakshinskiy BV, Ageev VN, Johnson RE (1998) Desorption of alkali atoms and ions from oxide surfaces: Relative to the origins of Na and K in atmospheres of Mercury and the Moon. J Geophys Res 103(E3):5873–5887
Matsuoka A, Yokota S, Murata N, Harada Y, Imajo S, Terada N, Keika K, Masunaga K, Sakai S, Nakagawa H, Asamura K, S Kasahara and Saito Y (this issue, under review) Magnetic field experiment at Phobos and in space around Mars by the Martian Moons eXploration (MMX) mission, Progress in Earth and Planetary Science
McComas DJ, Nordholt JE (1990) New approach to 3-D, high sensitivity, high mass resolution space plasma composition measurements. Rev Sci Instrum 61(10):3095. https://doi.org/10.1063/1.114169
McFadden JP et al (2015) MAVEN suprathermal and thermal ion compostion (STATIC) instrument, space. Sci Rev 195:199–256. https://doi.org/10.1007/s11214-015-0175-6
Michel P, Ulamec S, Boettger U, Grott M, Murdoch N, Vernazza P, Sunday C, Zhang Y, Valette R, Castellani R, Biele J, Tardivel S, Groussin O, Jorda L, Knollenberg J, Grundmann JT, Arrat D, Pont G, Mary S, Grebenstein M, Miyamoto H, Nakamura T, Wada K, Yoshikawa K, Kuramoto K (2022) The MMX rover: performing in-situ surface investigations on Phobos. Earth Planets Space 74:2
Mura A, Milillo A, Orsini S, Kallio E, Barabash S (2002) Energetic neutral atoms at Mars 2. Imaging of the solar wind-Phobos interaction. J Geophys Res 107(10):1278. https://doi.org/10.1029/2001JA000328
Nakamura T, Ikeda H, Kouyama T, Nakagawa H, Kusano H, Senshu H, Kameda S, Matsumoto K, Gonzalez-Franquesa F, Ozaki N, Takeo Y, Baresi N, Oki Y, Lawrence DJ, Chabot NL, Peplowski PN, Barucci MA, Sawyer E, Yokota S, Terada N, Ulamec S, Michel P, Kobayashi M, Sasaki S, Hirata N, Wada K, Miyamoto H, Imamura T, Ogawa N, Ogawa K, Iwata T, Imada T, Otake H, Canalias E, Lorda L, Tardivel S, Mary S, Kunugi M, Mitsuhashi S, Doressoundiram A, Merlin F, Fornasier S, Reess J-M, Bernardi P, Imai S, Ito Y, Ishida H, Kuramoto K, Kawakatsu Y (2021) Science operation plan of Phobos and Deimos from the MMX spacecraft. Earth Planets Space 73:227. https://doi.org/10.1186/s40623-021-01546-6
Pickett NB, McFadden JP, Fowler CM, Hanley KG, Benna M (2021) Carbon ion fluxes at mars: first results of Tailward flows From MAVEN-STATIC. J Geophys Res Space Phys 127(1):029635. https://doi.org/10.1029/2021JA029635
Pollock C et al (2016) Fast plasma investigation for magnetospheric multiscale. Space Sci Rev 199(1):331–406. https://doi.org/10.1007/s11214-016-0245-4
Poppe AR, Curry SM, Fatemi S (2016) The Phobos neutral and ionized torus. J Geophys Res Planets 121(5):770–783. https://doi.org/10.1002/2015JE004948
Rahmati A, Larson DE, Cravens TE, Lillis RJ, Dunn PA, Halekas JS, Connerney JE, Eparvier FG, Thiemann EMB, Jakosky BM (2015) MAVEN insights into oxygen pickup ions at Mars. Geophys Res Lett 42:8870–8876. https://doi.org/10.1002/2015GL065262
Saito Y, Yokota S, Asamura K, Tanaka T, Akiba R, Fujimoto M, Hasegawa H, Hayakawa H, Hirahara M, Hoshino M, Machida S, Mukai T, Nagai T, Nagatsuma T, Nakamura M, Oyama K, Sagawa E, Sasaki S, Seki K, Terasawa T (2008a) Low energy charged particle measurement by MAP-PACE onboard SELENE. Earth Planets Space 60:375–385. https://doi.org/10.1186/BF03352802
Saito Y, Yokota S, Tanaka T, Asamura K, Nishino MN, Fujimoto M, Tsunakawa H, Shibuya H, Matsushima M, Shimizu H, Takahashi F, Mukai T, Terasawa T (2008b) Solar wind proton reflection at the lunar surface: low energy ion measurement by MAP-PACE onboard SELENE (KAGUYA). Geophys Res Lett 35:L24205. https://doi.org/10.1029/2008GL036077
Saito Y, Yokota S, Asamura K, Tanaka T, Nishino MN, Yamamoto T, Terakawa Y, Fujimoto M, Hasegawa H, Hayakawa H, Hirahara M, Hoshino M, Machida S, Mukai T, Nagai T, Nagatsuma T, Nakagawa T, Nakamura M, Oyama K, Sagawa E, Sasaki S, Seki K, Shinohara I, Terasawa T, Tsunakawa H, Shibuya H, Matsushima M, Shimizu H, Takahashi F (2010) In-flight performance and initial results of plasma energy angle and composition experiment (PACE) on SELENE (Kaguya). Space Sci Rev 154(1–4):265–303. https://doi.org/10.1007/s11214-010-9647-x
Saito Y, Yokota S, Asamura K (2017) High speed MCP anodes for high time-resolution low-energy charged particle spectrometers. J Geophys Res 122(2):1816–1830. https://doi.org/10.1002/2016JA023157
Schaible MJ, Dukes CA, Hutcherson AC, Lee P, Collier MR, Johnson RE (2017) Solar wind sputtering rates of small bodies and ion mass spectrometry

detection of secondary ions. J Geophys Res Planets 122:1968–1983. https://doi.org/10.1002/2017JE005359
Senshu H, Mizuno T, Umetani K, Nakura T, Konishi A, Ogawa A, Ikeda H, Matsumoto K, Noda H, Ishihara Y, Sasaki S, Tateno N, Ikuse Y, Mayuzumi K, Kase T, Kashine H (2021) Light detection and ranging (LIDAR) laser altimeter for the Martian Moons Exploration (MMX) spacecraft. Earth Planets Space. https://doi.org/10.1186/s40623-021-01537-7
Tanaka T, Saito Y, Yokota S, Asamura K, Nishino MN, Tsunakawa H, Shibuya H, Matsushima M, Shimizu H, Takahashi F, Fujimoto M, Mukai T, Terasawa T et al (2009) First in situ observation of the Moon-originating ions in the Earth's magnetosphere by MAP-PACE on SELENE (KAGUYA). Geophys Res Lett 36:L22106. https://doi.org/10.1029/2009GL040682
Terada K, Yokota S, Saito Y, Kitamura N, Asamura K, Nishino MN (2017) Biogenic oxygen from Earth transported to the Moon by a wind of magnetospheric ions. Nat Astron 1:0026. https://doi.org/10.1038/s41550-016-0026
Usui T, Bajo KI, Fujiya W, Furukawa Y, Koike M, Miura YN, Sugawara H, Tachibana S, Takano Y, Kuramoto K (2020) The importance of Phobos sample return for understanding the Mars-moon system. Space Sci Rev 216:49. https://doi.org/10.1007/s11214-020-00668-9
Yokota S, Saito Y, Asamura K, Mukai T (2005) Development of an ion energy mass spectrometer for application on board three-axis stabilized spacecraft. Rev Sci Instrum 76:014501–014508
Yokota S, Saito Y, Asamura K, Tanaka T, Nishino MN, Tsunakawa H, Shibuya H, Matsushima M, Shimizu H, Takahashi F, Fujimoto M, Mukai T, Terasawa T (2009) First direct detection of ions originating from the Moon by MAP-PACE IMA onboard SELENE (KAGUYA). Geophys Res Lett 36:L11201
Yokota S, Tanaka T, Saito Y, Asamura K, Nishino MN, Fujimoto M, Tsunakawa H, Shibuya H, Matsushima M, Shimizu H, Takahashi F (2014) Structure of the ionized lunar sodium and potassium exosphere: dawn–dusk asymmetry. J Geophys Res 119(4):798–809. https://doi.org/10.1002/2013JE004529
Yokota S, Kasahara S, Mitani T, Asamura K, Hirahara M, Takashima T, Yamamoto K, Shibano Y (2017) Medium-energy particle experiments – ion mass analyzer (MEP-i) onboard ERG (Arase). Earth Planets Space 69:172. https://doi.org/10.1186/s40623-017-0754-8
Yokota S, Terada K, Saito Y, Kato D, Asamura K, Nishino MN, Shimizu H, Takahashi F, Shibuya H, Matsushima M, Tsunakawa H (2020) Global emissions of indigenous carbon ions from the Moon. Sci Adv 6:eaba1050. https://doi.org/10.1126/sciadv.aba1050
Yokota S, Terada N, Matsuoka A, Murata N, Saito Y, Delcourt D, Futaana Y, Seki K, Schaible MJ, Asamura K, Kasahara S, Nakagawa H, Nishino MN, Nomura R, Keika K, Harada Y, Imajo S (2021) In situ observations of ions and magnetic field around Phobos: the mass spectrum analyzer (MSA) for the Martian Moons eXploration (MMX) mission. Earth Planets Space 73:216. https://doi.org/10.1186/s40623-021-01452-x
Yokota S, Saito Y, Asamura K (2024) A low-energy particle experiment for both ion and electron measurements using a single microchannel plate-based detector. Earth, Planets Space 76:50. https://doi.org/10.1186/s40623-024-01997-7
Young DT, Bame SJ, Thomsen MF, Martin RH, Burch JL, Marshall JA, Reinhard B (1988) 2π-radian field-of-view toroidal electrostatic analyzer. Rev Sci Instrum 59:743. https://doi.org/10.1063/1.1139821

Publisher's Note